Journal of Modern Optics

3D-vortex labyrinths in the near field of solid-state microchip laser

A. Yu Okulov [a]
[a] P.N. Lebedev Physical Institute of Russian Academy of Sciences, Moscow, Russia

PLEASE SCROLL DOWN FOR ARTICLE

Taylor & Francis
Taylor & Francis Group

3D-vortex labyrinths in the near field of solid-state microchip laser

A. Yu Okulov*

P.N. Lebedev Physical Institute of Russian Academy of Sciences, Leninsky prospect 53, 119991, Moscow, Russia

The usage of vortex-labyrinth fields and Talbot lattices as optical dipole traps for neutral atoms is considered for the wavelength of trapping radiation in the range 0.98–$2.79\,\mu m$. The square vortex lattices generated in high Fresnel number solid-state microchip lasers are studied as a possible realization. The distribution of light field is obtained via a nonstationary computational model based on Maxwell–Bloch equations for a class-B laser, discrete Fox–Lee map with relaxation of inversion and a static model based on superposition of copropagating Gaussian beams. The spatial patterns obtained numerically and observed experimentally previously are interpreted as nonlinear superposition of vortices with helicoidal phase dislocations. The distribution of light field is approximated analytically by a sum of array of vortex lines and an additional parabolic subtrap. The separable optical trapping potential is proposed with similar intensity distribution. The factorization of the macroscopic wavefunction has led to the solution of the Gross–Pitaevsky equation for an ensemble of quantum particles trapped in a vortex labyrinth formed by a spatially periodic array of Laguerre–Gaussian beams.

1. Introduction

Optical dipole traps for neutral atoms (*1*) are a subject of considerable interest. A certain amount of proposals of increasing the complexity of trapping the EM field appeared recently. Apart from relatively simple geometrical patterns like standing plane-wave gratings (*2*), evanescent wave mirrors (*3*), toroidal traps which utilize the intensity distribution of Laguerre–Gaussian (LG) beams in the beam waist (*4*), several proposals were made which utilize the arrays of Gaussian beams, both phase-locked (*5*, *6*) and unlocked ones (*7*). The interference inherent to phase-locking provides multiply connected configurations of intensity distribution, phase gradients and electromagnetic (EM) momentum density (*8*, *9*). The winding EM momentum distribution is the cause of the angular momentum transfer to macroscopic bodies (e.g. dielectric ball) (*10*) and to trapped BEC as well (*11*).

The EM field configuration under consideration is based upon properties of self-imaging optical fields (*12*, *13*). The difference between a phase-locked array

---

*Email: okulov@sci.lebedev.ru

of zero-order Gaussian beams and a phase-locked array of optical vortices (OV) obtained experimentally in the near field of a solid-state microchip laser (*14*) is that the latter consists of an array of parallel vortex lines with opposite circulations and topological charges ℓ_{EM} (TC) (Figure 1) (*5*). In contrast to earlier proposals where individual loading and addressing of trapping sites was considered (*7*), this OV array has a sophisticated configuration of intensity (*5*) and EM momentum density of the trapping field. Due to this configuration the BEC trapped in the EM field might have a macroscopic wavefunction of complex form composed of an array of superfluid vortices (SFV). The cause of SFV formation is a light-induced torque experienced by an isolated resonant atom which interacts with a Laguerre–Gaussian beam having phase singularity. It was show by
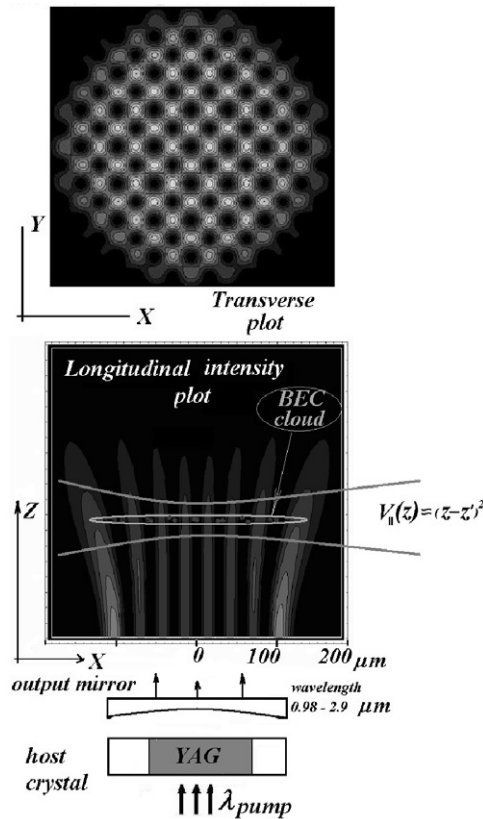
Figure 1. Conceptual view of the near-field optical trap. Upper plot: transverse (in the *XOY* plane) distribution of the intensity in the near field of a solid-state microchip laser (*5*). Middle: the longitudinal scale extends to six Talbot lengths. The *z* axis is directed along the optical axis of a microchip laser resonator (bottom). Additional tightly confined parabolic well keeping the BEC cloud localized in the *z* direction is depicted via the potential $V(z) \approx (z-z')^2$. Such a potential is assumed to be superimposed by the other microchip laser beam with a cylindrical focusing lens at a slightly different wavelength of the radiation from the range 0.98–2.79 μm, in order to avoid interference. The Fresnel number has a value of $N_f \approx N_{\text{vortices}}^2 = 64$.

Allen *et al.* (*8*) that the value of the torque at the saturation limit is $T = \hbar \ell_{EM} \Gamma$. The origin of this torque is due to a nonzero azimuthal EM momentum component. The azimuthal Doppler shift corresponding to such a motion had been observed (*9*). This torque might have an appreciable value even in the nonresonant case, although it is significantly reduced by a multiple of $(\Delta/\Gamma)^2$, where Δ is the detuning and Γ is the linewidth (*8*). As a result an azimuthal component of EM momentum is transferred to an atom in such a way that it will move around the phase singularity – the direction of rotation is fixed by TC of the trapping beam. This is the cause of the circular motion of BEC confined in an isolated toroidal trap.

In the current paper the maximally transparent and simple analytical description presented describes the transfer of angular momentum from an optical vortex array (OVA) to a trapped BEC. As a first step in section 2, the distribution of light intensity and phase in the near field of a solid-state microchip laser are computed. The configuration of the intensity and the phase of an EM field of OVA has a complicated, multinode structure. In sections 3 and 4 the spatially periodic arrays of Gaussian and Laguerre–Gaussian beams of the first order are compared. Next, in section 5, in order to get an analytic solution for the macroscopic wavefunction Ψ trapped by an optical vortex array, a special optical pancake-like potential (Figure 1) will be constructed. In this trapping potential the separation of variables in the Gross–Pitaevsky Equation (2) becomes possible. Next the procedure applied previously to an elongated sech^2-profile optical trap (*15*) will be used. Due to a special adjustment of the potential, it is possible to capture an analytic approximation for Ψ in the form of a superposition of the elementary equispaced vortices. The topological charges and angular momenta of adjacent vortices are counter-directed in contrast to a 'rotating bucket' trap where angular momenta of SFV in a bucket are co-directed (*16*, *17*). The numerical modelling via a split-step FFT technique will be performed to check this approximate formula. The obtained spatial distribution of the Ψ modulus and argument will be used for the analysis of a classical field of velocities of a trapped atom. The complex form of the constructed macroscopic wavefunction Ψ trapped by an optical vortex array might be interesting from the point of view of diminishing the decoherence induced by the environment in topological quantum computing (*18*).

2. Square vortex lattices

Recent advances in controlling the dynamics of solid-state microchip lasers (*14*) offer the possibility of reliable control of spatiotemporal optical patterns. Compared to semiconductor lasers the host medium composed of dielectric crystal doped by neodimium Nd^{+3} or other rare earth ions (Er^{+3}, Tm^{+3}, Ho^{+3}, Yb^{+3}) have smaller gain and smaller self-phase modulation. Because of smaller nonresonant losses the heating of the host crystal by radiation is not dramatic. The changes of the geometry and birefrigence of host crystals, curvature and reflectivity of output couplers and spatial distribution of optical pumping give efficient control over the mode structure. The square vortex lattices (SVL) observed in the quasi-plane parallel cavity (*14*) are of special interest. These lattices demonstrate a high degree of spatial coherence: the relaxation oscillations of a class-B high Fresnel number solid-state microchip laser (*14*) with Fresnel number in the

range $N_f \approx 100-1000$ are characterized by a single peak at a frequency about $[(T_1 \tau_c)^{1/2}]^{-1}$ $(0.3-1.2 \, \text{MHz})$. This is firm evidence of a single-longitudinal and single transverse mode behaviour. The former theoretical analysis was based on a parabolic equation, resulting from adiabatic elimination of polarization from a standard set of Maxwell–Bloch equations (19):

$$\frac{\partial E(\mathbf{r}, t)}{\partial t} + \frac{E(\mathbf{r}, t)}{\tau_c} + \frac{ic}{2k} \Delta_\perp E(\mathbf{r}, t) = \frac{\sigma c N_0 L_a E(\mathbf{r}, t)(1 + i\delta\omega T_2)}{2L_r (1 + \sigma T_1 c\epsilon_0 |E|^2/\hbar\omega)}, \tag{1}$$

where τ_c is the photon lifetime in the cavity, $k = 2\pi/\lambda$ is the wavenumber, σ is the stimulated emission cross-section, $\delta\omega$ is the detuning of the lasing frequency from the center of the gain line, N_0 is the density of inverted resonant atoms per unit volume, T_1 is the inversion lifetime (longitudinal relaxation lifetime), L_a is the thickness of the active medium, L_r is the length of the resonator, c is the speed of light, ϵ_0 is the dielectric constant, and $\Delta_\perp = \nabla_\perp^2$ (20). When finite gain linewidth T_2^{-1} is taken into account in the framework of the Swift–Hohenberg equation:

$$\frac{\partial E(\mathbf{r}, t)}{\partial t} + \frac{E(\mathbf{r}, t)}{(\tau_c + T_2)} + \frac{i\tau_c c}{2k(\tau_c + T_2)} \Delta_\perp E(\mathbf{r}, t)$$
$$- \frac{T_2^2}{\tau_c(\tau_c + T_2)^2} \left(\frac{\tau_c c}{k} \Delta_\perp + \delta\omega T_2\right)^2 E(\mathbf{r}, t) = \frac{\sigma c N_0 L_a E(\mathbf{r}, t)(1 + i\delta\omega T_2)}{2L_r (1 + \sigma T_1 c\epsilon_0 |E|^2/\hbar\omega)}, \tag{2}$$

the square vortex lattices were obtained numerically (21). The additional term with the square of the transverse laplacian is responsible for the transverse mode selection due to finite gain linewidth. An alternative model with discrete time step equal to $\tau = 2 L_r/c$ (time of bouncing of radiation between mirrors) utilizes the standard rate equations of the class-B laser written at the nth step for the electric field (5, 22):

$$E_{n+1}(\mathbf{r}) = f(E_n(\mathbf{r})) = \frac{\sigma L_a N_n(\mathbf{r}) E_n(\mathbf{r})(1 + i\delta\omega T_2)}{2} + E_n(\mathbf{r}), \tag{3}$$

inversion:

$$N_{n+1}(\mathbf{r}) = N_n(\mathbf{r}) + \left[\frac{N_0(\mathbf{r}) - N_n(\mathbf{r})}{T_1} - \sigma N_n(\mathbf{r}) c\epsilon_0 |E_n|^2/\hbar\omega\right] \frac{2L_r}{c}, \tag{4}$$

and nonlocal integral mapping evaluating the field via fast Fourier transform at each timestep:

$$E_{n+1}(\mathbf{r}) = \int_{-\infty}^{\infty} \int_{-\infty}^{\infty} K(\mathbf{r} - \mathbf{r}') f(E_n(\mathbf{r}')) \, \mathrm{d}^2\mathbf{r}'. \tag{5}$$

The kernel K for the nearly plane-parallel Fabry–Pérot cavity of microchip laser with transverse filtering via aperture $D(\mathbf{r}')$ has the form (12):

$$K(\mathbf{r} - \mathbf{r}') = \frac{ikD(\mathbf{r}')}{2\pi L_r} \exp[ik(\mathbf{r} - \mathbf{r}')^2/2L_r]. \tag{6}$$

The following parameters were chosen for the numerical simulation: $T_1 = 2 \times 10^{-4}$ s, $L_r = 1 \, \text{mm}$, for Nd^{+3}-doped crystals, $\sigma = (1.2 - 0.6) \times 10^{-20}$ cm^2, $N_0 = 10^{16}$ cm^{-3},

$\delta\omega T_2 = 0.1$. In the numerical evaluation of Equation (5) via the split-step FFT method (23) the mesh size in the X, Y plane was 512×512 points. The 'guard bands ratio' (24) was set equal to 8. The main part of the field Ψ was located inside the central part of a mesh of 64×64 size – the 'image area'. The tolerance of the energy spillover was kept within $\epsilon_1 = 0.001$. The 'windowing' in wavenumber space after FFT at each timestep was performed by use of the 'Fermi–Dirac' smoothed step function (23). The dissipation inherent to 'windowing' in the split-step FFT method was compensated by the nonlinear gain. The initial conditions for field E_n were taken as the multimode random field (23).

Just near the lasing threshold the radiation mode has a distribution of intensity as a rectangular grating of bright and dark spots: the latter are vortex cores. The nonlocal integral mapping proved to be successful in computation of the near field distribution as well. Quite unexpectedly in most runs the parallel vortex lines were obtained (Figure 1) (5) rather than a periodic array of bright and dark spots, typical to the Talbot phenomenon (12). The origin of parallel vortex lines is interpreted as the nonlinear superposition of vortices with helicoidal phase dislocations. In the next section and section 4 the possibility of an approximation of this nonlinear optical vortex lattice by a linear equivalent will be outlined.

3. Talbot lattices

Consider a phase-locked rectangular lattice of zero-order Gaussian beams located at sites $\mathbf{r}_{jx, jy}$ (12) separated by period p, where jx, jy are the discrete indices corresponding to the x and the y coordinate of a given site. Let us assume for simplicity that polarization is linear, thus the spin of light is zero. At the $z = 0$ plane the electric field E is given by the expression

$$E(\mathbf{r}, 0) = E_0 \sum_{jx, jy} \exp[-|\mathbf{r} - \mathbf{r}_{jx, jy}|^2/(2d^2)]. \tag{7}$$

After paraxial propagation of distance z the electric field $E(\mathbf{r}, z)$ is transformed into

$$E(\mathbf{r}, z) = E_0 \frac{i \exp[ikz]}{(1 - iz/kd^2)} \sum_{jx, jy} \exp\left[-\frac{|\mathbf{r} - \mathbf{r}_{jx, jy}|^2}{2d^2(1 - iz/(kd^2))}\right]. \tag{8}$$

The constructive interference between adjacent beams produces periodic interference patterns in different z-spaced planes. The initial periodical pattern is reproduced at so-called Talbot distances $z_t = 2 \, p^2/\lambda$. In the intermediate planes $z_t/4m$ the coarser lattices with periods p/m are produced (23, 24). As a result a 3D lattice of bright spots is formed (Figure 2).

Each spot could serve as a potential well for neutral atoms (1, 2, 5, 6), because the intensity gradient will attract or repulse the atomic dipoles depending on the sign of the detuning of the radiation frequency from resonance. At low frequencies (red-detuning) the atomic dipole oscillates in-phase with the trapping field and tries to align parallel to the electric field. Thus, the potential energy of the dipole $U = -\mathbf{p} \cdot \mathbf{E}(\mathbf{r})/2$ is lower in the local maxima of the intensity and the atoms are collected at bright spots. On the other hand, at frequencies above the resonance (blue-detuning), the atomic dipole oscillates out-of-phase

and it has the tendency to align anti-parallel to the electric field. In this blue-detuned case the potential energy of the dipole is higher in the local maxima of the intensity and atoms are repelled into the dark regions.

Such geometry of trapping in integer and fractional Talbot planes based on superposition of co-propagating zeroth-order Gaussian beams was considered earlier (5) including the possibility of the manipulation of optical lattice geometry via mutual polarization (6) of constituting beams.

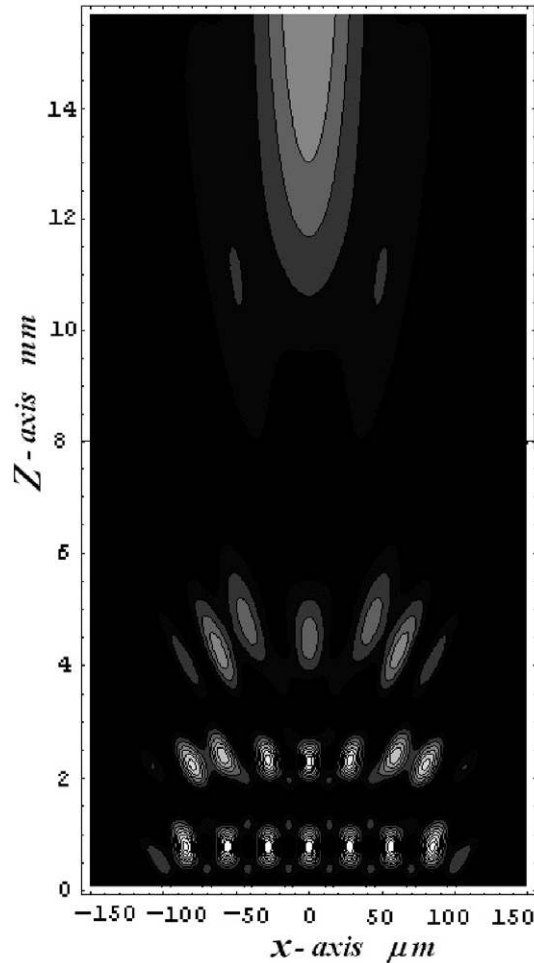Figure 2. Diffractive self-imaging of a two-dimensional lattice of 8×8 Gaussian beams with period $p = 28\,\mu$m. The longitudinal cross-section at the $y = 0$ plane of the intensity distribution $I(x, y, z)$ is presented. The lattice is self-reproduced at the Talbot distance, spatial period division occurs at a quarter Talbot distance and the central lobe forms outside the Rayleigh range.

4. Artificial vortex labyrinth

Consider now the periodic array of Laguerre–Gaussian vortex beams with helicoidal phase dislocations (Figure 3):

$$E(\mathbf{r}, z = 0) \approx E_0 \sum_{jx,\,jy} (|\mathbf{r} - \mathbf{r}_{jx,\,jy}|) \exp\left(-|\mathbf{r} - \mathbf{r}_{jx,\,jy}|^2/d^2\right)$$

$$\times \exp\left(-|\mathbf{r}|^2/D^2\right) \, \exp[i\ell_{EM} \, \mathrm{Arg}(\mathbf{r} - \mathbf{r}_{jx,\,jy}) + i\pi(jx + jy)]. \tag{9}$$

The topological charge ℓ_{EM} is assumed to be unity, the neighbouring beams (components of the sum (9)) are π-shifted. The apodization function $\exp\left(-|\mathbf{r}|^2/D^2\right)$ is added in order to suppress the maximum of the interference pattern at the edge of array. The beam centers are placed in the center of the rectangular grid $\mathbf{r}_{jx,\,jy}$ of period p whose axes are parallel to X, Y. The overlapping beams produce an interference pattern formed by two arrays of bright and dark spots rotated at a $45°$ angle with respect to the initial array of LG beams. The dark spots are of two kinds: one lattice of spots coincides with a lattice of initial vortices (9), the other one is produced by interference and it is shifted at distance $p/2^{1/2}$ along the diagonal of the initial lattice. The resulting interferogram has an apparent $45°$ tilt compared to the lattice of the initial vortices (Figure 3).
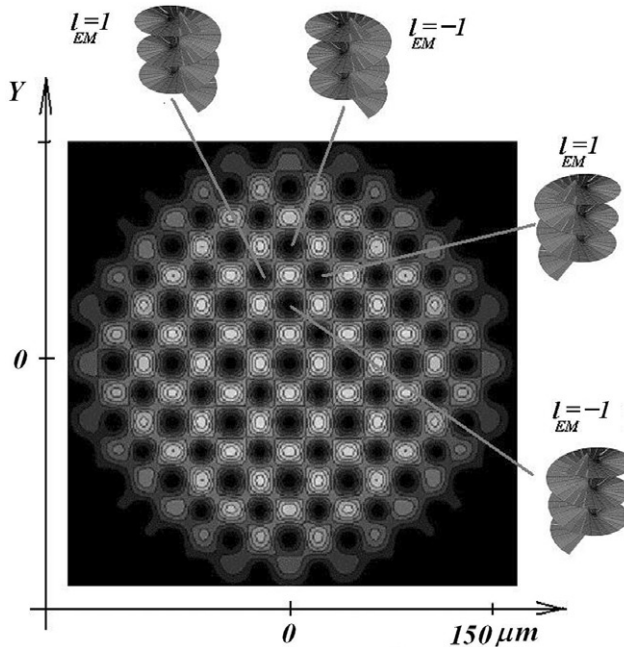

Figure 3. Intensity distribution in the transverse plane of an artificial Laguerre–Gaussian vortex array. The vortices (dark holes) are at the nodes of a rectangular *chessboard-like* grid. Letters ℓ_{EM} denote vortices with alternating topological charges, changing sign from one site of the lattice to another.

The topological charges of dark spots (vortices) flip from one site to another. The interesting feature of this interference pattern is the distribution of the angular momentum (*13*). The initial array of LG beams carries unit circulation and the corresponding angular momentum at each site. Such a *chessboard-like* interferogram (Figure 3) contains an additional array of vortices with alternative charges. The net angular momentum tends to be close to zero, because at the central part of the array each positively directed TC ℓ_{EM} is compensated by four adjacent negative ones having charge $-\ell_{EM}$. The elementary cell of such a lattice consists of two π-shifted initial vortices with co-directed charges ℓ_{EM} located at diagonal and two counter-directed charges $-\ell_{EM}$ (π-shifted too) placed at the other diagonal of the cell. The period p of the initial pattern in the numerical recipes (*5*) was taken as 30 μm while the width of each initial beam was set to $w_{LG} = 22$ μm in order to provide significant mutual overlapping of the vortices.

The longitudinal distribution of the intensity of the optical vortex array is composed of periodically spaced (with period p) hollow tubes – vortex cores (Figure 4). Apart from Talbot gratings which are reproduced by diffraction at the $z_t = 2p^2/\lambda$ planes with corresponding period division in between the planes, the vortex array under consideration keeps its shape within the Rayleigh range, i.e. at distances $z < D^2/\lambda$. Within this distance the diameter of the cores is kept constant along z by virtue of the interference of the adjacent vortices, whose helical wavefronts are perfectly matched within the elementary cell (Figure 5).

Consider now the interaction of individual atoms with a single optical beam carrying a topological charge. The gradient force will attract the 'red'-detuned atomic dipole to the intensity maximum of an isolated first-order Laguerre–Gaussian beam – 'doughnut' beam (Figure 5), i.e. to the ring-shaped area around the phase singularity. As a result the cloud of the cold atoms will be accumulated near the maximum of the intensity or 'doughnut', as follows from the variational solution of the Gross–Pitaevsky equation (GPE) (*2*):

$$i\hbar \frac{\partial \Psi(\mathbf{r}, t)}{\partial t} = -\frac{\hbar^2}{2m} \Delta \Psi(\mathbf{r}, t) + V_{ext}(\mathbf{r})\Psi(\mathbf{r}, t)$$

$$+ \frac{4\pi\hbar^2 a}{m} \Psi(\mathbf{r}, t)|\Psi(\mathbf{r}, t)|^2, \tag{10}$$

with trapping potential V_{ext} of the form

$$V_{ext}(\mathbf{r}) = \frac{m\omega_z^2 z^2}{2} - \text{Re} \, [\alpha(\omega)]|E_0|^2[r^2 \, \exp(-r^2/(2w_{LG}^2))], \tag{11}$$

where $\alpha(\omega)$ is the polarizability of the atom (*1*), m is the mass of the particle and a is the scattering length.

The approximate variational solution of the GPE for the ground state macroscopic wavefunction is the Laguerre–Gaussian function (*11*):

$$\Psi(\mathbf{r}, t) = |\mathbf{r}| \, \exp(-|\mathbf{r}|^2/(2w_r^2) - z^2/(2w_z^2) + i\ell_{BEC}\phi), \tag{12}$$

where ℓ_{BEC} is the topological charge of this vortex Ψ solution. Hence, the probability distribution $|\Psi(\mathbf{r}, t)|^2$ of finding an atom somewhere near the point $\mathbf{r} = (x, y, z)$ at the moment t is similar to the intensity distribution of the trapping field as pointed out in (*11*).
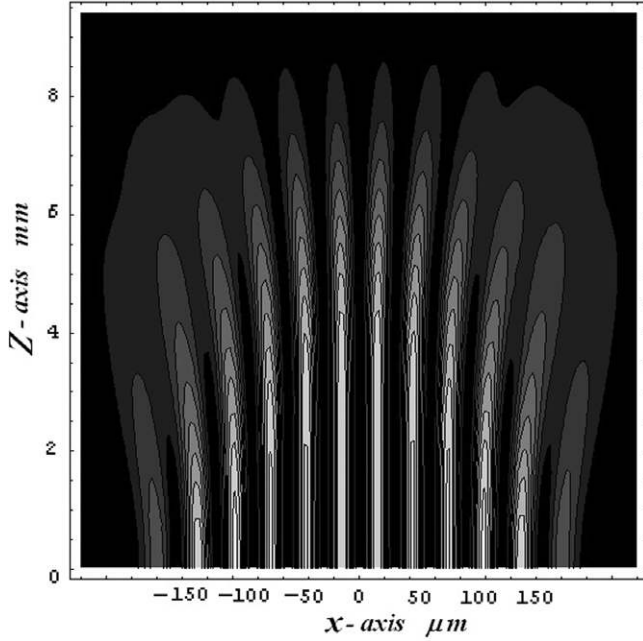
Figure 4.   Longitudinal section of the vortex array in the near field in the *x*–*z* plane at the $y = 0$ section. The vortex lines are parallel, and the topological charges ℓ_{EM} are flipping from one vortex line to another. The wavelength $\lambda = 1 \, \mu m$ and the period p of the lattice both in the *x* and the *y* directions is $30 \, \mu m$.

More information could be obtained from the study of the phase structure of the wavefunction and comparison of the topological charges of the trapping field and the BEC vortex. It is easy to realize using the Madelung transform

$$\Psi(\mathbf{r}, t) = [\rho(|\mathbf{r}|, \phi, t)]^{1/2} \exp(i\theta(|\mathbf{r}|, \phi, t)), \tag{13}$$

that there exists flow of 'probability fluid' with velocity **v** proportional (parallel) to the phase gradient lines:

$$v(\mathbf{r}, t) = \frac{\hbar}{m} \nabla\theta(\mathbf{r}, t). \tag{14}$$

Such 'flow of wavefunction' occurs around the *z* axis (beam axis). The 'flow' described by (12) is potential and conservative as it should be for a superfluid. This picture is complicated by the vorticity of the EM momentum, inherent to LG beams (9). Strictly speaking the rotation of the classical dipole around the core is accelerated by the nonconservative torque induced by the azimuthal force circulating around the vortex core. For a two-level atom the value of the torque *T* is given by the following expression obtained by Babiker *et al.* (8):

$$T = \hbar\ell_{EM}\Gamma\left[\frac{I_L}{1 + I_L + \Delta^2/\Gamma^2}\right], \tag{15}$$
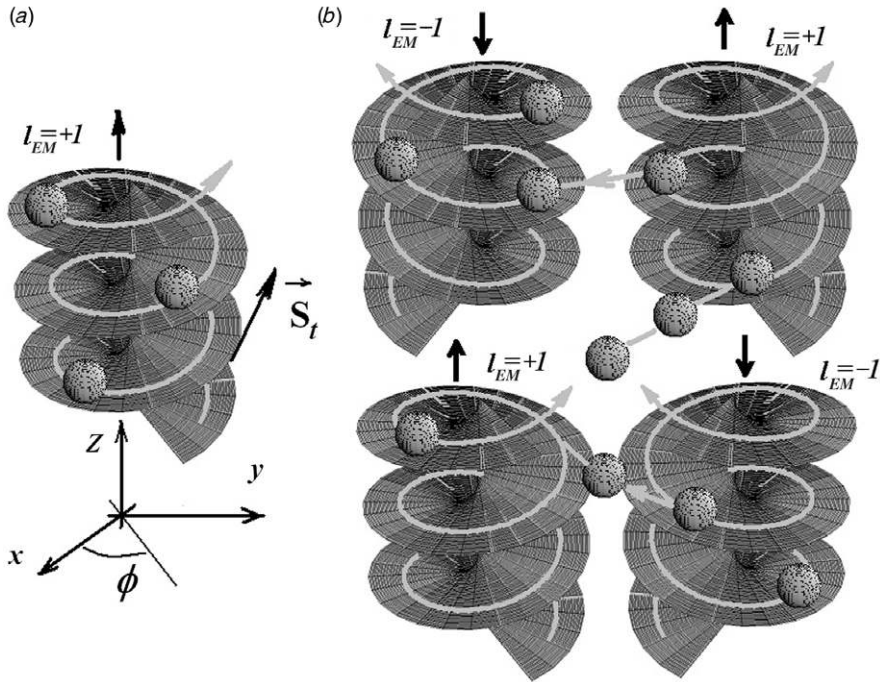
Figure 5. (*a*) Helicoidal phase surface of the Laguerre–Gaussian beam. An atomic dipole having 'red' detuning moves along the phase gradient. The trajectory is located at the maximum of the intensity. $\mathbf{S}_t$ is the component of the Pointing vector tangential to the helix. The major component of $\mathbf{S}_z$ is directed parallel to the beam propagation, i.e. along the *z* axis. (*b*) Helicoidal phase surface of the Laguerre–Gaussian beam array. The elementary cell consists of four vortices. The adjacent vortices have alternating topological charges ℓ_{EM} and alternating angular momenta. In the classical picture the atomic dipole moves along the phase gradient of a given vortex; next it jumps to another one.

where I_L is the normalized trapping field intensity, $\varDelta = \omega - \omega_0$ is the detuning of the trapping field frequency ω from the resonant frequency ω_0 of the dipole. In the saturation limit T is simply: $T = \hbar \ell_{EM} \Gamma$. In the nonresonant case this torque reduces as $\Gamma^2/\varDelta^2$. At trapping frequencies of the Nd^{+3} laser $\varDelta = 10^{14}$ Hz and for the GaAs laser with $\varDelta = 10^{13}$ Hz and the *D*-line doublet of ^{85}Rb with linewidth $\Gamma = 5 \times 10^6$ Hz (*1*), the torque is reduced by a factor depending on the laser intensity I_L. Thus, due to trade-off between the saturation and detuning, the torque exists both near and at large detuning from the resonance. Consequently the loop integral of the azimuthal force over the circular trajectory around the core $\oint (\mathbf{F_t} \times \mathbf{r}) \cdot d\mathbf{l}$ is nonzero (Figure 5).

In the classical picture because of this torque, the dipole placed in the doughnut beam will move 'upwards' on the helicoidal phase staircase, i.e. it will rotate around the LG-beam axis. The direction of rotation is determined by the topological charge ℓ_{EM} of the trapping beam (Figure 5). Qualitatively the classical dipole is pushed by the azimuthal periodic electric field – it happens because the phase of the electric field oscillations at each point in the circle around the center of the beam is shifted with respect to the

neighbouring points. Thus, classical dipole placed at the maximum of the intensity of the GL beam will feel the 'plane-wave-like' nonresonant pressure of the light field. The associated azimuthal Doppler shift of the moving atom was observed experimentally recently (26). Outside the resonance, the origin of the torque T is interpreted in a similar way: the Pointing vector has a component $S(\mathbf{r})_t$ tangential to the helix and the local flux of the electromagnetic momentum pushes the dipole along the phase gradient, i.e. in the azimuthal direction. The local density of the EM momentum $\mathbf{g} = \mathbf{S}/c^2$ is proportional to the components of the Pointing vector (9):

$$S(\mathbf{r})_t = \frac{\epsilon_0 \omega \ell_{\mathrm{EM}} c^2}{r} |E(\mathbf{r})|^2$$
$$S(\mathbf{r})_z = \epsilon_0 c |E(\mathbf{r})|^2, \tag{16}$$

where $S(\mathbf{r})_t$ is the tangential component of the Pointing vector, $S(\mathbf{r})_z$ is the axial one, $|(\mathbf{r})|$ is the distance from the optical vortex core, and ω is the frequency of the trapping field. The existence of the tangential component of the Pointing vector became visible when the macroscopic dielectric ball with radius larger than the LG-beam core and comparable to the 'doughnut' radius is placed in the center of the LG-beam. The rotation of the particle is induced via such a torque and the corresponding transfer of the angular momentum (10).

When loaded in the optical vortex lattice (Figure 6) the atomic dipole will move around the adjacent vortex core with acceleration. The radius of the rotation will increase until the dipole approaches the separatrices of the velocity fields. Next, after a certain amount of rotations around the vortex core, it could jump to another vortex using the bright areas between the vortices as a bridge (Figure 3). This qualitative picture is complicated by the azimuthally inhomogeneous distribution of the intensity around each core.

Our aim now is to show that the just described classical motion has a quantum mechanical counterpart. The transfer of the angular momentum results in the specific form of the macroscopic wavefunction Ψ maintaining coherence all over the trapping array:

$$\Psi(\mathbf{r}) \approx \sum_{jx, jy} (|\mathbf{r} - \mathbf{r}_{jx, jy}|) \exp(-|\mathbf{r} - \mathbf{r}_{jx, jy}|^2/d^2)$$
$$\times \exp(-|\mathbf{r}|^2/D^2) \exp[i\ell_{\mathrm{BEC}} \, \mathrm{Arg} \, (\mathbf{r} - \mathbf{r}_{jx, jy}) + i\pi(jx + jy)]. \tag{17}$$

The next section presents the method for the solution of the Gross–Pitaevsky equation with the vortex trapping field $E(\mathbf{r})$ in the form (9).

5. Separable vortex array potential for BEC

In order to get a closed form solution for macroscopic Ψ it is worth mentioning that the azimuthal accelerating force has a very small value, falling as Δ^{-2} under detuning from resonance (8). Next let us introduce the optical potential V_{ext} as a square modulus of the trapping field $E(\mathbf{r}_\perp, z)$ (1). The torque T will be taken into account as a 'selection' rule for choosing the distribution of the topological charges l_{BEC} in the resulting solution.
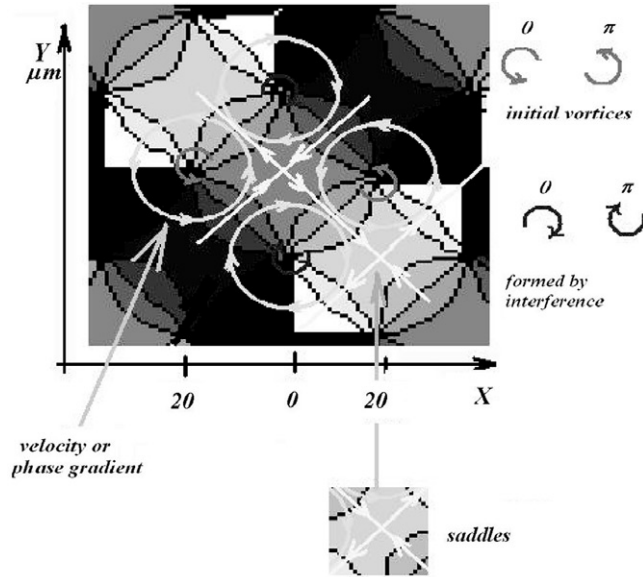
A. Yu Okulov

Figure 6.   The argument of macroscopic wavefunction Ψ and corresponding field of velocities obtained via the Madelung transform. The superfluid vortices form the lattice with alternating topological charges $\ell_{BEC} = \pm 1$. The elementary cell consists of four BEC vortices whose locations are identical to the vortices of the trapping EM field. The horizontal pair has the same charges ℓ_{BEC} which are π-shifted with respect to each other, the vertical pair has π-shifted $-\ell_{BEC}$ charges. The alternating charges ℓ_{BEC} make the field of velocities continuous.

It was shown recently (*15*) that the Gross–Piaevsky equation (*2*) in a 3D configuration:

$$i\hbar \frac{\partial \Psi(\mathbf{r}, t)}{\partial t} = -\frac{\hbar^2}{2m} \Delta \Psi(\mathbf{r}, t) + V_{\text{ext}}(\mathbf{r})\Psi(\mathbf{r}, t)$$
$$+ \frac{4\pi\hbar^2 a(\mathbf{B})}{m} \Psi(\mathbf{r}, t)|\Psi(\mathbf{r}, t)|^2, \tag{18}$$

admits the application of the standard method of separation of the variables widely used for the solution of a *linear* partial differential equation, e.g. in quantum mechanics. The separation of the variables means that the wavefunction is factorized:

$$\Psi(\mathbf{r}, t) = \Psi_\perp(\mathbf{r}_\perp, t)\Psi_{||}(z, t) \tag{19}$$

provided the Hamiltonian is the sum of two components. The first component depends on a longitudinal variable z and the second component depends upon the transverse variables $\mathbf{r}_\perp$.

Following (*15*) in order to separate the variables and factorize the wavefunction, let us choose a trapping potential in the following form, as a sum of components depending on
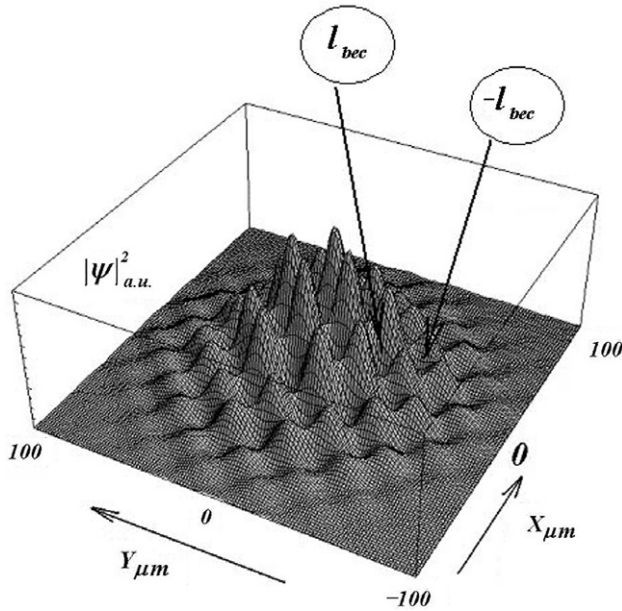
Figure 7. The distribution of the square modulus of the macroscopic wavefunction Ψ obtained via numerical modelling. The location of adjacent counter-rotating vortices ℓ_{BEC} are shown.

the longitudinal coordinate z and the transverse coordinates $\mathbf{r}_\perp$ separately:

$$V_{ext}(\mathbf{r}_\perp, z) = V_z + V_\perp = \frac{m\omega_z^2 z^2}{2} - \text{Re}\left[\alpha(\omega)\right]|E(\mathbf{r}_\perp)|^2 \\ + \frac{m\omega_\perp^2 |(\mathbf{r}_\perp)|^2}{2}, \tag{20}$$

where $\alpha(\omega)$ is the atomic polarizability (1):

$$\alpha(\omega) = 6\pi\epsilon_0 c^3 \frac{\Gamma/\omega_0^2}{(\omega_0^2 - \omega^2 - i(\omega^3/\omega_0^2)\Gamma)}. \tag{21}$$

The $\alpha(\omega)$ is assumed to be real due to the large negative ('red') detuning from the atomic resonance at frequency $\omega_0 = 2.4 \times 10^{15}$ Hz. The imaginary part of the denominator under detuning $\Delta = \omega - \omega_0$ for ^{85}Rb atoms trapped by the EM field at $\lambda = 0.808 - 1.06\,\mu$m is $(3 - 4.7) \times 10^8$ times smaller than the real part, so the permittivity of the atom $\alpha(\omega)$ is real with good accuracy (1). The trapping field $E(\mathbf{r}_\perp)$ is assumed to be a periodic function of the transverse variables $\mathbf{r}_\perp = (x, y)$, composed of the LG beams placed at the nodes (jx, jy) of a rectangular grid of period p (9).

The additional parabolic well with frequency $\omega_\perp$ is introduced in (20) to get an analytical solution for the one trapping vortex. In order to avoid the interference between

the different trapping beams, the use of different carrier frequencies is recommended for the longitudinal parabolic well $m\omega_z^2 z^2/2$, the vortex array beam $E(\mathbf{r})$ and the parabolic subtrap in (20). The characteristic scales of the potential in the longitudinal direction and transverse direction are chosen to form a 'pancake trap': $\omega_z \gg \omega_\perp$ (Figure 1). The opposite case of the elongated trap with $\omega_z \ll \omega_\perp$ and the 'solitonic' longitudinal potential $V_z \approx \mathrm{sech}^2(z)$ was considered earlier using an analogous procedure (15).

The longitudinal part of the wavefunction $\Psi_\parallel(z, t)$ is obtained as a ground state of the 1D harmonic oscillator:

$$i\hbar \frac{\partial \Psi_\parallel}{\partial t} = -\frac{\hbar^2}{2m} \frac{\partial^2 \Psi_\parallel}{\partial z^2} + \frac{m\omega_z^2 z^2}{2} \Psi_\parallel, \tag{22}$$

$$\Psi_\parallel = \left(\frac{m\omega_z}{\pi\hbar}\right)^{1/4} \exp[-m\omega_z z^2/(2\hbar) - i\omega_z t]. \tag{23}$$

The transverse part of the wavefunction $\Psi_\perp(\mathbf{r}_\perp, t)$ is to be obtained by solving the 'transverse' GPE:

$$i\hbar \frac{\partial \Psi_\perp}{\partial t} = -\frac{\hbar^2}{2m} \Delta_\perp \Psi_\perp + V_\perp(\mathbf{r}_\perp)\Psi_\perp$$
$$+ \frac{4\pi\hbar^2 a(\mathbf{B})}{m} \Psi_\perp |\Psi_\perp|^2 \left[\int_{-\infty}^{\infty} |\Psi_\parallel(z, t)|^4 \, dz\right] \Big/ \left[\int_{-\infty}^{\infty} |\Psi_\parallel(z, t)|^2 \, dz\right], \tag{24}$$

where

$$V_\perp = \frac{m\omega_\perp^2 |\mathbf{r}_\perp|^2}{2} - \mathrm{Re}\ [\alpha(\omega)]|E(\mathbf{r}_\perp)|^2. \tag{25}$$

Because of normalization

$$\int_{-\infty}^{\infty} |\Psi_\parallel(z, t)|^4 dz = 1/2 \quad \text{and} \quad \int_{-\infty}^{\infty} |\Psi_\parallel(z, t)|^2 dz = 1. \tag{26}$$

The following 2D GPE results from separation of variables for the 'pancake' trap:

$$i\hbar \frac{\partial \Psi_\perp}{\partial t} = -\frac{\hbar^2}{2m} \Delta_\perp \Psi_\perp + V_\perp(\mathbf{r}_\perp)\Psi_\perp + \frac{2\pi\hbar^2 a(\mathbf{B})}{m} \Psi_\perp |\Psi_\perp|^2. \tag{27}$$

The scattering length a as a function of the magnetic field is

$$a(\mathbf{B}) = a_{\mathrm{bg}}\left(1 + \frac{\Delta_B}{B - B_R}\right), \tag{28}$$

where Δ_B is a width of the Feshbach resonance, B_R is the resonant magnetic field and a_{bg} is the background scattering length (2).

Formally the separation of the variables is applicable each time when the Hamiltonian is a sum of the components depending on the different groups of variables, but this method has additional physical meaning for asymmetric potentials. The examples are elongated in the z direction trap (15) and the 'pancake' 2D trap (Figure 1) as in the current case.

The dynamics of Ψ in the 2D traps has been considered in a large number of papers, including the geometries of the periodic potentials, Bessel lattices etc. In the current case, the SFV lattice under consideration has some features, qualitatively described above in the discussion of classical motion of the dipole around the phase singularity.

The continuous transfer of the angular momentum from the optical vortex to the BEC with wavefunction Ψ might induce vortices in an initially nonrotating BEC. Because the direction of rotation of the classical particle is determined by the distribution of TC of the optical vortices ℓ_{EM} of the trapping beam, the distribution of TCs in a quantum superfluid lattice ℓ_{BEC} will be set identical to those of the trapping field.

The possible solution of Equation (27) presumes the identical spatial distributions for fields $\Psi_\perp(\mathbf{r}_\perp, t)$ and $E(\mathbf{r}_\perp)$. It means that Ψ is also a sum of LG functions with alternating topological charges ℓ_{BEC} (see Equation (17)). Unfortunately, the effective diameter of the core b is much larger than the effective size of the LG-beam bottleneck (4–10 μm). However, this discrepancy does affect the basic features of the solution because of the logarithmic dependence of the vortex energy on the vortex dimensions (*17*).

The correlation K of two complex spatially inhomogeneous fields $\Psi_\perp(\mathbf{r}_\perp, t)$ and $E(\mathbf{r}_\perp)$ is expected to be equal to unitary:

$$K = \frac{|\int \Psi_\perp E^*(\mathbf{r}_\perp)\, \mathrm{d}^2 \mathbf{r}_\perp|^2}{[\int |\Psi_\perp|^2\, \mathrm{d}^2 \mathbf{r}_\perp][\int |E(\mathbf{r}_\perp)|^2\, \mathrm{d}^2 \mathbf{r}_\perp]} = 1. \tag{29}$$

The key point is in adjusting the parameters in $\Psi_\perp(\mathbf{r}_\perp, t)$ and $E(\mathbf{r}_\perp)$ in such a way that the two last terms in (24) cancel each other. This might happen when the following condition is imposed upon the coefficients:

$$\mathrm{Re}\,[\alpha(\omega)]|E_0|^2 = \frac{2\pi\hbar^2 a(\mathbf{B})}{m}. \tag{30}$$

The mutual compensation of these two terms could be achieved via tuning of the magnetic field $\mathbf{B}$ near the Feshbach resonance.

Consider first the case of a single vortex trap collocated with a single parabolic subtrap:

$$V_\perp = \frac{m\omega_\perp^2 r^2}{2} - \mathrm{Re}\,[\alpha(\omega)]|E_0|^2 r^2 \exp[-r^2/d^2]. \tag{31}$$

The following exact solution for the 2D harmonic oscillator is known:

$$\Psi_\perp = \left(\frac{2}{\pi}\right)^{1/2}\left[\frac{m\,\omega_\perp}{\hbar}\right]^{3/2} r\, \exp\left[-\frac{m\,\omega_\perp^2 r^2}{2\hbar} + i\,\phi\,\ell_{BEC} - i\,2\,\omega_\perp t\right], \tag{32}$$

which is similar to the variational solution for the 'transverse' wavefunction (12) (*11*). Note in our case the exact wavefunction of the transversal GPE is found, rather than the variational one (12). The stability analysis will be published elsewhere. The angular

A. Yu Okulov

momentum per particle is given by

$$\langle \hat{\ell} \rangle = \iint \Psi_\perp^* (-i\hbar) \frac{\partial \Psi_\perp}{\partial \phi} \, \mathrm{d}^2 \mathbf{r}_\perp = \hbar \tag{33}$$

where ϕ is the azimuthal angle (Figure 5). Again SFV carries the angular momentum $\hbar$ per particle and kinetic energy of the whole vortex line $E_{\mathrm{kin}} = \rho \, \pi \, \hbar^2 \, \chi \, \ln \, (\tilde{b}/\tilde{a})/m$ (17). Consider now the trapping of the BEC by phase-locked Gaussian–Laquerre beams placed at the nodes ix, jx of a rectangular grid of period p (see Equation (9)).

Let us assume for simplicity that the optical wavelength λ is equal to the de Broglie wavelength λ_{db}:

$$\lambda = \lambda_{\mathrm{db}} = \frac{\hbar}{(2 \, m \, k_{\mathrm{B}} T)^{1/2}} . \tag{34}$$

The corresponding BEC temperature for ^{85}Rb atoms is

$$T = 1.7^{-7} \text{ K}. \tag{35}$$

After imposing compensation condition (26) the residual part of transverse GPE (27) corresponds to free-space evolution:

$$i \hbar \frac{\partial \Psi_\perp}{\partial t} = -\frac{\hbar^2}{2m} \varDelta_\perp \Psi_\perp + \frac{m \omega_\perp^2 r^2}{2} \Psi_\perp . \tag{36}$$

The free space propagation (Figure 1) equation for the EM field will be of similar form:

$$\frac{\partial E}{\partial z} = -\frac{i}{2 \, k} \varDelta_\perp E + \frac{k r^2}{2 f_{\mathrm{cavity}}} E , \tag{37}$$

where f_{cavity} is the effective focal length of the laser cavity (Figure 1) induced by the thermal lens collocated with the inhomogeneity of the optical pumping.

Because of the linearity of the equation and the superposition principle, the solution of (37) will be the sum of free-space modes including zero-order Gaussian functions, Gaussian–Hermit or Laguerre–Gaussian modes located at sites $\mathbf{r}_{jx,jy}$ (12) separated by period p. The axes of such an optical array are parallel to X, Y. In order to solve numerically Equation (27) the split-step FFT method (23) was used. The mesh size in the X, Y plane was 512×512 points; the 'guard bands ratio' (24) was chosen equal to 8. So the main part of the field Ψ was located inside the central part of a mesh which was 64×64 in size – the 'image area'. The tolerance of the energy spillover was kept within $\epsilon_1 = 0.0001$. The windowing in wavenumber space after FFT at each timestep was performed by use of the 'Fermi–Dirac' smoothed step function (23). The dissipation inherent to the split-step FFT method has led to a decrease of the total 'amount of particles' $\iint |\Psi|^2 \, \mathrm{d}x \, \mathrm{d}y$ within the 'image area' at a speed of 10^{-3} per timestep. The special initial conditions of the 'preselected' SFV array in the form (17) superimposed upon the homogeneous background gave the spatial distribution (Figure 7) of the 'transverse' wavefunction $\Psi_\perp$ well correlated ($K \approx 0.7$) with the OVA array distribution – the array of the phase-locked

Gaussian–Laguerre wavepackets of the first order:

$$\Psi_\perp = \frac{2}{\pi}\left[\frac{m\omega_\perp}{\hbar}\right]^{3/2}\sum_{jx,\,jy}(|\mathbf{r}-\mathbf{r}_{jx,\,jy}|)\,\exp(-|\mathbf{r}|^2/D^2)\,\exp\left[-\frac{m\omega_\perp{}^2|\mathbf{r}-\mathbf{r}_{jx,\,jy}|^2}{2\hbar}\right.$$

$$\left. +\,i\ell_{\mathrm{BEC}}\,\mathrm{Arg}\,(\mathbf{r}-\mathbf{r}_{jx,\,jy})+i\pi(jx+jy)-i2\omega_\perp t\right]. \tag{38}$$

Thus, the numerical solution for $\Psi_\perp$ of the GPE proved to be very close to the linear combination of the Gaussian–Laguerre functions. Nevertheless, this solution takes into account the interference between wavefunctions of the 'subvortices', because the 'doughnut' radius is set to be a bit more than the distance between the lattice nodes. The arising interference pattern is well correlated with the interference pattern produced by the Laguerre–Gaussian OVA $|E(\mathbf{r}_\perp)|^2$ (Figure 3) with the same geometrical parameters and wavelength λ. This solution proved to be stable with respect to small harmonic perturbations.

Each SFV carries angular momentum $\hbar$ per particle and rotational kinetic energy $E_{\mathrm{kin}}=\rho\pi\hbar^2\chi\ln(\tilde{b}/\tilde{a})/m$, where $\tilde{b}$ is the diameter of the vortex core, $\tilde{a}$ is the interatomic distance and χ is the length of the vortex which is roughly equal to the thickness of the 'pancake' (17). The energy associated with the superfluid vortices is of order $10^{-(19-20)}J$ or 0.1–1 eV at the density of dilute ^{85}Rb gas $\rho\approx10^{16-18}\,\mathrm{cm}^{-3}$. In contrast to a superfluid in a rotating bucket where the angular momenta of the vortices are co-directed (16), the BEC vortices trapped by an optical vortex array are counter-directed from site to site. Consequently in the net sum of the angular momenta each vortex of positive topological charge is compensated by the term with negative charge and the total angular momentum tends to zero. Nevertheless, the mutual subtraction of angular momenta (vectorial) of adjacent vortices in the net sum does not mean the mutual subtraction of rotational energies, which are the positive scalars. The ground state carries a substantial amount of rotational kinetic energy of the condensate which contains N particles of mass m per unit volume, namely $E_{\mathrm{rot}}=N_{\mathrm{vortices}}\rho\pi\hbar^2\chi\ln(\tilde{b}/\tilde{a})/m$.

6. Conclusion

The optical vortex arrays emitted by a solid-state microchip laser were analysed from the point of view of the application to optical dipole traps. Firstly the numerical modelling of a thin slice microchip Fabry–Pérot solid-state laser resonator gave transverse field distributions (Figure 3) well correlated with that experimentally observed previously. The longitudinal intensity distribution consists of a periodically spaced array of parallel hollow tubes which slowly diverge while propagating along the z axis (Figure 4). The array of phase-locked Gaussian–Laguerre beams equispaced at the nodes of a rectangular lattice proved to be a reasonable approximation for the experimental as well as the numerical results.

For macroscopic wavefunction Ψ of a BEC trapped in such a complex optical field, the analytical solutions of the Gross–Pitaevsky equation were found. These solutions are

based upon the separation of variables and mutual compensation of the vortex component of an external trapping field via the nonlinear term of the GPE. The obtained wavefunctions have perfect correlation with the trapping field, including distribution of the topological charges, which form an 'antiferromagnetic-like' lattice. Within the framework of this particular model the 'antiferromagnetic' lattice of the BEC vortices carries a total angular momentum close to zero while the net rotational kinetic energy of the SFV lattice tends to be equal to the sum of the rotational energies of the vortices. Geometrically such a BEC cloud looks like a 'pancake' perpendicular to the z axis.

The field of classical velocities, i.e. the field of phase gradients, obtained via the Madelung transform, forms a 'labyrinth' structure. It means that the trapped atoms move in the 'pancake' plane, i.e. the x–y plane. The rotation of an atom around some vortex core is accelerated by the EM torque. The radius of the rotation is gradually increased. When the particle reaches the separatrix, it comes to another vortex area. The trajectory of the particle in the transverse plane (x–y plane) is Mobius-like: because the number of optical vortices is finite, in the classical picture the particle will return to the initial vortex eventually after roaming for some time inside a trapping 'labyrinth'.

In the quantum picture represented via the analytic solution of the GPE for one trapping vortex and the numerical solution for an optical vortex array, the coherent macroscopic wavefunction extends all over the OV trapping array with a transverse spatial dimension of several hundred microns. The complex field of velocities, rotational energy and high degree of correlation of the SFV wavefunction with the OV trapping field promise more resistance to the decoherence.

The qualitative analytic solution supports the basic feature related to the trapping of macroscopic particles and to BEC trapping: the transfer of OAM from an optical field to a superfluid. The proposed OVA trap might be interesting from the point of view of studies of the quantum classical correspondence.

The mechanism of imposing the topological charges to BEC vortices by means of manipulating the vorticity of a trapping optical array could result in the demonstration of macroscopic quantum interference phenomena. Evidently there are four possible topologically equivalent combinations of the parameters of solution (38) of the OV charges ($\ell_{EM} = \pm 1$) and their relative phases ($\pm\pi$). Thus, there exist four wavefunctions Ψ having an identical probabability $|\Psi|^2$ distribution and different orientation of the SFL vortices with respect to the physical axes x, y of the trapping setup, characterized by ℓ_{BEC} and their relative phases. The transformation of one Ψ into another one which has a different phase structure is equivalent to a 90° rotation around the z axis.

References

(1) Grimm, R.; Weidemuller, M.; Ovchinnikov, Yu.B. *Adv. At. Mol. Opt. Phys.* **2000**, *42,* 95.
(2) Pitaevskii, L.; Stringari, S. *Bose–Einstein Condensation*; Clarendon Press: Oxford, 2003; Dalfovo, F.; Giorgini, S.; Stringari, S.; Pitaevskii, L.P.; Rev. Mod. Phys. **1999**, *71,* 463–512 (1999).
(3) Balykin, V.I.; Letokhov, V.S.; Ovchinnikov, Yu.B.; Sidorov, A.I. *Phys. Rev. Lett.* **1988**, *60,* 2137–2140.
(4) Wright, E.M.; Arlt, J.; Dholakia, K. *Phys. Rev. A* **2001**, *63,* 013608-1–013608-7.

(5) Okulov, A.Yu. *QCMC-2004, AIP Conf. Proc.* **2004**, *734,* 366–369 A. Yu. Okulov, Bull. Lebedev Phys. Inst. **2003,** *9,* 3–9.

(6) Ovchinnikov, Yu.B. *Phys. Rev. A* **2006**, *73,* 033404-1–033404-10.

(7) Dumke, R.; Volk, M.; Muther, T.; Buchkremer, F.B.J.; Birkl, G.; Ertmer, W. *Phys. Rev. Lett.* **2002**, *89,* 097903-1–097903-4.

(8) Babiker, M.; Power, W.L.; Allen, L. *Phys. Rev. Lett.* **1994**, *73,* 1239–1242.

(9) Garces-Chavez, V.; McGloin, D.; Padgett, M.J.; Dultz, W.; Schmitzer, H.; Dholakia, K. *Phys. Rev. Lett.* **2003**, *91,* 093602-1–093602-4.

(10) Friese, M.J.; Euger, J.; Rubinstein-Dunlop, H. *Phys. Rev. A* **1996**, *54,* 1543–1596; Heckenberg, N.R.; Friese, M.E.J.; Nieminen, T.A.; Rubinstein-Dunlop, H. Mechanical Effects of Optical Vortices. In *Optical Vortices*, Eds.; Vasnetsov, M. Nova Science Publishers: New York, 1999; pp 75–105.

(11) Tempere, J.; Devreese, J.T.; Abraham, E.R.I. *Phys. Rev. A* **2002**, *64,* 023603-1–023603-8.

(12) Okulov, A.Yu. *JOSA B* **1990**, *7,* 1045–1050.

(13) Courtial, J.; Zambrini, R.; Dennis, M.R.; Vasnetsov, V. *Opt. Express* **2006**, *14,* 938–944.

(14) Chen, Y.F.; Lan, Y.P. *Phys. Rev. A* **2001**, *64,* 063807–1.063807-5 Y.F. Chen, Y.P. Lan, *Phys. Rev. A.* **2001**, *65,* 013802-1–013802-6.

(15) Fidele, R.; Shukla, P.K.; De Nicola, S.; Manko, M.A.; Manko, V.I.; Cataliotti, F.S. *JETP Lett.* **2004**, *80,* 609–614.

(16) Abo-Shaerr, J.R.; Raman, C.; Vogels, J.M.; Ketterle, W. *Phys. Rev. Lett.* **2002**, *88,* 070409-1–070409-4; Danaila, I. *Phys. Rev. A* **2005**, *72,* 013605–1–013605-6.

(17) Feynman, R.P. *Statistical Mechanics* Addison-Wesley: Reading, MA, 1972; Chapter 11.

(18) Kitaev, A.Yu. [Online]; 1997 LANL e-print quant-ph/ 9707021, http://arxiv.org (accessed Sep 7, 2004).

(19) Suchkov, A.F. *JETP* **1965**, *22,* 1026–1034.

(20) Siegman, A.E. *Lasers* University Science Books: Mill Valley, CA, 1986.

(21) Staliunas, K. *Phys. Rev. A* **1993**, *48,* 1573–1581, Staliunas, K.; Weiss, C.O. *JOSA B* **1995**, *12* 1142–1150.

(22) Hollinger, F.; Jung, Chr.; Weber, H. *JOSA B* **1990**, *7,* 1013–1020.

(23) Okulov, A.Yu. *Opt. Commun.* **1993**, *99,* 350–354, *J. Mod. Opt.* **1991,** *38,* 1887–1889.

(24) Okulov, A.Yu. *Opt. Spectrosc.* **1994**, *77,* 985–991.

(25) Sziklas, E.A.; Siegman, A.E. *Appl. Opt.* **1975**, *14,* 1874–1890.

(26) Garces-Chavez, V.; Volke-Sepulveda, K.; Chavez-Cerda, S.; Sibbett, W.; Dholakia, K. *Phys. Rev. A* **2002**, *66,* 063402-1–063402-8.